



Bismuthene - Tetrahedral DNA nanobioconjugate for virus detection

Estefanía Enebral-Romero^{a,b}, Daniel García-Fernández^b, Laura Gutiérrez-Gálvez^b, David López-Diego^c, Mónica Luna^c, Adrián García-Martín^{f,g}, Elena Salagre^{f,g}, Enrique G. Michel^{f,g}, Íñigo Torres^{d,e}, Félix Zamora^{d,e}, Tania García-Mendiola^{b,e,**}, Encarnación Lorenzo^{a,b,e,*}

^a IMDEA-Nanociencia, Ciudad Universitaria de Cantoblanco, 28049, Madrid, Spain

^b Departamento de Química Analítica y Análisis Instrumental. Universidad Autónoma de Madrid, 28049, Madrid, Spain

^c Instituto de Micro y Nanotecnología IMN-CNM, CSIC (CEI UAM+CSIC), Isaac Newton 8, Tres Cantos, 28760, Madrid, Spain

^d Departamento de Química Inorgánica and Condensed Matter Physics Center (IFIMAC). Universidad Autónoma de Madrid, 28049, Madrid, Spain

^e Institute for Advanced Research in Chemical Sciences (IAChem). Universidad Autónoma de Madrid, 28049, Madrid, Spain

^f Departamento de Física de la Materia Condensada, Facultad de Ciencias, Universidad Autónoma de Madrid, Madrid, Spain

^g Condensed Matter Physics Center (IFIMAC), Universidad Autónoma de Madrid, Madrid, Spain

ARTICLE INFO

Keywords:

Nanostructured bioconjugate
Tetrahedral DNA nanostructure (TDN)
SARS-CoV-2 aptamer-based tetrahedral DNA nanostructure (TDNapt)
Aptasensor
Bismuthene nanosheets

ABSTRACT

In this work, we present an electrochemical sensor for fast, low-cost, and easy detection of the SARS-CoV-2 spike protein in infected patients. The sensor is based on a selected combination of nanomaterials with a specific purpose. A bioconjugate formed by Few-layer bismuthene nanosheets (FLB) and tetrahedral DNA nanostructures (TDNs) is immobilized on Carbon Screen-Printed Electrodes (CSPE). The TDNs contain on the top vertex an aptamer that specifically binds to the SARS-CoV-2 spike protein, and a thiol group at the three basal vertices to anchor to the FLB. The TDNs are also marked with a redox indicator, Azure A (AA), which allows the direct detection of SARS-CoV-2 spike protein through changes in the current intensity of its electrolysis before and after the biorecognition reaction. The developed sensor can detect SARS-CoV-2 spike protein with a detection limit of 1.74 fg mL^{-1} directly in nasopharyngeal swab human samples. Therefore, this study offers a new strategy for rapid virus detection since it is versatile enough for different viruses and pathogens.

1. Introduction

During the last few years, a new tendency leading to the development of fast and easy-to-use diagnostic tools has risen exponentially. This approach is supported by the increasing demands for a simpler, faster, and higher quality healthcare system from the society. To overcome this problem, the determination of pathogens such as viruses or bacteria is one of the most critical challenges that must be solved. Traditionally, pathogens have been identified using different methodologies such as antibody-based immunoassays, mass spectroscopy, and polymerase chain reaction (PCR) techniques (Nehra et al., 2022). These methods present limitations like long analysis times, high cost, complex equipment, etc. (Hameed et al., 2018). Various innovative methodologies are being developed to overcome these issues, highlighting electrochemical techniques that bring advantages like rapid detection, high

selectivity, and low detection limits (Ahmadivand and Gerislioglu, 2022; Hartati et al., 2021).

Among these methodologies, electrochemical biosensors that employ aptamers as the recognition element have recently appeared as a competitive method because of their selectivity and sensitivity besides the rapid analysis, low cost, and portability (Li et al., 2022). The use of aptamers, short single-stranded RNA or DNA oligonucleotides with high stability that bind specifically to a wide range of targets (proteins, nucleic acids, metal ions, etc.), brings important advantages such as their adaptability, versatility, and easiness of use (Hartati et al., 2021). In aptasensor development, the immobilization of the aptamer on the electrode is one of the most crucial steps (Enebral-Romero et al., 2023; Mishra et al., 2022; Mugo et al., 2021; Zambry et al., 2022). In this sense, the use of bioconjugates improve the aptamer immobilization strategy and increase sensibility. The use of bioconjugates in the development of

* Corresponding author. IMDEA-Nanociencia, Ciudad Universitaria de Cantoblanco, 28049, Madrid, Spain.

** Corresponding author. Departamento de Química Analítica y Análisis Instrumental. Universidad Autónoma de Madrid. 28049, Madrid, Spain
E-mail address: tania.garcia@uam.es (E. Lorenzo).

<https://doi.org/10.1016/j.bios.2024.116500>

Received 20 March 2024; Received in revised form 29 May 2024; Accepted 12 June 2024

Available online 13 June 2024

0956-5663/© 2024 The Authors. Published by Elsevier B.V. This is an open access article under the CC BY-NC license (<http://creativecommons.org/licenses/by-nc/4.0/>).

biosensors is usual (Bai et al., 2012; Hartati et al., 2021; Roushani and Shahdost-fard, 2017; Wang et al., 2020) and brings some advantages such as simplicity and rapidness. Thus, a new approach, based on the use of nanostructured bioconjugates, is proposed in this work.

Nanostructured bioconjugates are one of the most promising fields of research in terms of sensing. These structures result from combining nanomaterials and biomolecules, showing better properties than the individual materials due to their synergistic effect. Any biologically active molecule can be combined with a nanomaterial for bioconjugate preparation, including aptamers. Concerning nanomaterials, 2D nanomaterials with electrical conductivity, fast electron transfer kinetics, large surface area, and easy functionalization are ideal for developing novel electrochemical biosensors (Su et al., 2019). Bismuthene is one of the most innovative identified 2D nanomaterials, and its use for sensing applications is currently emerging. Monolayer and few-layer bismuthene have attracted the scientific community's attention due to their outstanding properties, including biocompatibility, chemical and thermal stability, exceptional metallic properties, and light-material solid interactions (Gutiérrez-Gálvez et al., 2024; Torres et al., 2022). However, its application for biosensing is yet to be exploited and even more so its interaction with biomolecules to form nanohybrids with specific properties.

Recently, the use of nucleic acids as building blocks for preparing nanostructures rather than molecules carrying genetic information has been demonstrated to be very useful in biosensing field (García Fernández et al., 2023). Indeed, two approaches have been used so far: *i*) DNA Origami, based on the folding of a long DNA single strand with the help of staple strands (Rothemund, 2006), and *ii*) the preparation of three-dimensional polyhedral nanostructures based on base complementarity (Gutiérrez-Gálvez et al., 2024). This second approach is more interesting, as it allows to form stable, resistant, and versatile three-dimensional structures by selectively positioning functional groups of different natures at the nanometric level, which is difficult to achieve in other types of nanomaterials (Bujold et al., 2018). Among these polyhedral structures, tetrahedral DNA nanostructures (TDNs) stand out not only for their characteristics but also for their high reaction yields, rigidity (Lo et al., 2010), and the possibility of being functionalized with biomolecules at the upper vertex that act as a capture probe allowing the analyte biorecognition. In contrast, the basal vertices can be modified with different functional groups, such as thiol group, that facilitate anchoring to all type of surfaces.

Moreover, these tetrahedral DNA nanostructures can be combined with dyes or redox indicators, introducing electrochemical properties. Redox indicators are electroactive molecules with high chemical stability of both the oxidized and reduced species, a reversible redox response, low toxicity, and mainly interact in a different extension with double-stranded and single-stranded DNA. Hence, they have been widely employed in DNA biosensors to detect the hybridization event. However, as far as we know, they do not have been used to detect the biorecognition reaction between the aptamer and the target protein.

Taking everything mentioned above into account, in this work we have labelled tetrahedral DNA nanostructures (TDNs) with an electroactive phenothiazine (Azure A), that has been used as electrochemical indicator to detect hybridization (Martínez-Periñán et al., 2021; Pina-Coronado et al., 2022), and we have prepared for the first time a nanostructured bioconjugate between the Azure A labelled TDNs and few-layer bismuthene (FLB) for the development of an electrochemical aptasensor for direct detection of SARS-CoV-2. The Azure A (AA) adsorbed on the nanostructure acts as a redox indicator of the biorecognition reaction between the aptamer included in the bioconjugate and the target analyte, the SARS-CoV-2 spike protein. The analyte detection by Differential Pulse Voltammetry (DPV) is a simple and fast methodology that does not need complex equipment. Moreover, this method is versatile and can be applied to detect other pathogens if needed.

2. Material and methods

2.1. Reagents, solutions, and apparatus

2.1.1. Reagents

Dibasic sodium phosphate, monobasic sodium phosphate, sodium chloride, magnesium chloride, tris(hydroxymethyl)aminomethane (TRIS, $\text{NH}_2\text{C}(\text{CH}_2\text{OH})_3$), Azure A, RBD SARS-CoV-2 thiolated aptamer sequence and tetrahedral DNA nanostructure sequences, and interferent proteins (p53, IgG and CEA) shown in Table S1, were purchased from Merck (<https://www.merckgroup.com/>). SARS-CoV-2 RBD recombinant spike protein (SARS-CoV-2 S¹ protein) was supplied by Sino Biological Europe GmbH (Eschborn, Germany). Bismuth trichloride (BiCl_3 , 99.999%), dodecanethiol (DDT, 99.9%), and octadecene (ODE, 90%) were from Alfa Aesar. Oleylamine (OA, 70%), from Sigma Aldrich.

2.1.2. Apparatus

Atomic Force Microscopy (AFM) measurements were carried out using a Cervantes Fullmode AFM from Nanotec Electronica SL. WSxM software (www.wsxmsolutions.com) was employed for data acquisition and image processing (Gimeno et al., 2015; Horcas et al., 2007). AFM contact mode was used to acquire all the topographical images to avoid possible artifacts in the flake thickness measurements (Nemes-Incze et al., 2008). PPP-NCHR cantilevers (nanosensors.com) with a nominal spring constant of 42 N/m and tip radius of less than 7 nm were employed. Low forces of the order of 1 nN were used for imaging to ensure that the tip would not deform the flakes.

X-Ray Powder Diffraction (XRPD) was used for FLB characterization. PXRD patterns were measured on a Bruker D8 Advance with Cu K α radiation with a rapid detector (lynxeye).

Raman spectroscopic characterization of FLB was carried out on a confocal Raman microscope with a spectral resolution of 0.02 cm^{-1} , coupled with an AFM instrument (Witec ALPHA 300 R A), with laser excitation at 532 nm and a 100 \times objective lens (NA = 0.95). The incident laser power was 0.5 mW. The optical diffraction resolution was about 200 nm laterally and 500 nm vertically. The samples were mounted in a piezo-driven scan platform with 4 nm lateral and 0.5 nm vertical positioning accuracy, also equipped with an active vibration isolation system (0.7–1000 Hz). The spectra and images were processed and analyzed with the WiTec Project Plus 2.08 software.

Transmission Electron Microscopy (TEM) images were obtained in a JEOL JEM 2100 FX TEM system with an accelerating voltage of 200 kV. The microscope has a multiscan charge-coupled device (CCD) camera ORIUS SC1000 and an OXFORD INCA X-Ray Energy Dispersive Spectroscopy (XEDS) microanalysis system. For the preparation of TEM samples, the product obtained by centrifugation was dispersed in CHCl_3 and deposited on lacey formvar/carbon copper grids (300 mesh).

Few-layer bismuthene nanolayers Scanning Electron Microscopy (SEM) images were acquired in an FE-SEM Hitachi S-4700 operating at an accelerating voltage of 20 kV.

All instrumentation used for SARS-CoV-2 aptamer-based tetrahedral DNA nanostructure (TDNapt) synthesis and characterization are described in the Supporting Information (SI).

For the nanostructured bioconjugate preparation, 3 KDa Centrifugal Filter Units and a Hettich Zentrifugen Universal 320 R centrifuge purchased from Merck were used.

For Raman characterization of each step in the development of the aptasensor the Bruker Senterra confocal Raman microscope (Bruker Optic, Ettlingen, Germany) was used. The optimal parameter applied to record the spectra were: 20 \times objective; 532 nm, 20 mW laser excitation; a resolution of 3–5 cm^{-1} ; 10 s of integration time; 5 co-additions and 50 \times 1000 μm slit opening.

UV-Visible spectra were recorded using a UV-1900 from SHIMADZU spectrophotometer using a 1 cm optical path quartz cell.

Fluorimetric measurements were performed in a Varian Cary Eclipse spectrofluorometer with 1 cm optical pitch quartz cuvettes.

Electrochemical measurements were performed in an Autolab/PGSTAT 10 potentiostat from EcoChemie controlled with GPES 4.9 software. Baseline corrections on Differential Pulse Voltammograms were done with the GPES 4.9 program. Screen-Printed electrode Connector was used as an interface, and Carbon Screen-Printed Electrodes (CSPEs) used in this work were provided by Metrohm (www.metrohm.com/es-es).

Atomic Force Microscopy (AFM) images were acquired with a Nanotec Electronic AFM system, in jumping mode, using silicon cantilevers (PPP-FM Nanosensors, 2.8 N/m nominal spring constant and 75 kHz resonant frequency). WSxM software was used for data acquisition and image processing (Horcas et al., 2007). SEM images and EDX spectra were taken at 2 kV and with a current of 13 pA, using a Scanning Electron Microscope VERIOS 460 from FEI. Fluorescence microscopy was performed with an incident light microscope Axioskop 2 MAT (ZEISS), implemented with a mercury short arc lamp HBO 50 W/AC L1 (OSRAM).

X-Ray Photoemission Spectroscopy (XPS) experiments were conducted in an ultrahigh vacuum (UHV) chamber with a pressure of less than $1 \cdot 10^{-9}$ mbar at room temperature. Core level spectra were obtained using a double anode X-ray source (Specs) with emission lines Mg K α (1253.6 eV) and Al K α (1486.6 eV). The Phoibos 150 electron analyzer was used as the detector, with its axis aligned with the surface normal. The core level binding energies were calibrated using the binding energies of C 1s and Au 4f in contact with the sample as references. The line shape of core levels is fitted using a Shirley background and asymmetric singlet pseudo-Voigt functions. The fit is optimized using a Levenberg-Marquardt algorithm with a routine running in IGOR Pro (WaveMatrix Inc.) (Schmid et al., 2014). The quality of the fit is judged from a reliability factor, the normalized χ^2 .

Purified water Millipore Milli-Q system (18.2 M Ω cm) was used to prepare all the solutions. All solutions and materials were sterilized in a Nüve OT012 autoclave.

2.1.3. Procedures

2.1.3.1. Few-layer bismuthene synthesis. FLB nanosheets were prepared following a slight modification of the previously reported procedure (Torres et al., 2022), see Fig. S1. Thus, BiCl₃ (315 mg, 1.00 mmol) was added under argon conditions in a 100 mL three-necked flask, followed by a DDT (4.00 mL) addition step and a vacuum step for the total salt solution. Then, ODE (6.00 mL) is added under argon conditions, and the solution is degassed under vacuum for 1 h at 60 °C. The yellow solution obtained is heated at 150 °C for 3 h under argon. After that, OA (1.00 mL) is added to the solution, reacting for 90 min at 150 °C. The resultant suspension is diluted with chloroform (40.0 mL), and centrifuged at 8000 rpm for 3 min, and the solid washed three times with 50.0 mL of chloroform, centrifuging again for 3 min at 8000 rpm. Finally, the solid is isolated and dried under a vacuum.

2.1.3.2. SARS-CoV-2 aptamer-based tetrahedral DNA nanostructure synthesis. The process followed for the tetrahedral DNA nanostructure preparation has already been optimized by the research group (Gutiérrez-Gálvez et al., 2024), see Fig. S2. Briefly, equimolar amounts of the four oligonucleotides to obtain a 1.00 μ M TDNapt (Tetra A-apt, Tetra B, Tetra C, and Tetra D) were mixed in TM buffer (20.0 mM Tris, 50.0 mM MgCl₂ pH 8.0) and introduced into a thermocycler. The synthesis is divided into three stages of 2 min. In the first stage, temperature was initially at 95 °C, then decreased to 51 °C. The second stage with decreasing temperatures of 46.1 °C, 43.6 °C 41.2 °C and 38.8 °C. And the last stage is divided into two steps of 30 °C and 4 °C.

2.1.3.3. Azure A solution. 10.0 mM stock solution of Azure A was prepared by dissolving the corresponding amount of Azure A (2.92 mg) in 1 mL of sterilized Milli-Q water. From this stock solution, a new Azure A

1.00 mM solution was prepared.

2.1.3.4. Nanostructured bioconjugate (FLB-TDNapt-AA) preparation. For the preparation of the FLB-TDNapt-AA nanostructured bioconjugate, first, 100 μ L of the synthesized TDNapt (1.00 μ M) were mixed with 100 μ L of Azure A (1.00 mM) and left for 1 h in the dark. Then, the unbound molecules were separated by filtration with a 3K filter in a centrifuge at 10,000 rpm for 10 min. A washing step was carried out with sterilized Milli-Q water and filtered again under the same conditions until the volume was halved. On the other hand, the FLB resuspended in isopropanol was filtered until all the solvent was removed, and then water was added to resuspended again the solid retained in the filter by a sonication step. Finally, 100 μ L the TDNapt-AA and 100 μ L of the FLB were mixed and left overnight in the absence of light. The next day it was filtered at 7000 rpm for 3 min, and the FLB-TDNapt-AA bioconjugate was obtained.

2.1.3.5. Aptasensor development and SARS-CoV-2 detection. Once the nanostructured bioconjugate was prepared, CSPEs were modified by drop casting with 10.0 μ L of the nanostructured bioconjugate and left overnight at room temperature in dark conditions. Then, the biosensing platform (CSPE/FLB-TDNapt-AA) was washed with purified water. Afterward, it was incubated, under controlled humidity, with 10.0 μ L of SARS-CoV-2 S¹ protein at different concentrations for 1 h at 37 °C. The electrode was rewashed with purified water and allowed to dry under ambient conditions before starting the electrochemical measurement. Finally, Differential Pulse Voltammograms (DPVs) were registered in PB 0.1M pH 7.0 as electrolyte.

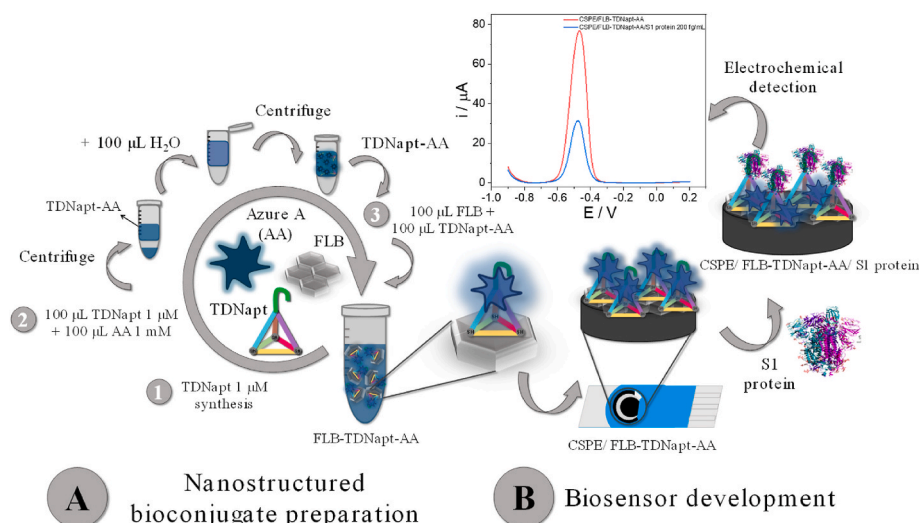
2.1.3.6. Detection of SARS-CoV-2 S¹ protein in nasopharyngeal swab samples. Nasopharyngeal swab samples were spiked with 50.0 fg mL⁻¹ and 100 fg mL⁻¹ concentration of SARS-CoV-2 S¹ protein from a stock one of 1.00 pg mL⁻¹ using PBS 10.0 mM pH 7.0 as solvent. Then, 10.0 μ L of the solution was incubated on the CSPE/FLB-TDNapt-AA electrochemical platform for 1 h at 37 °C. Finally, electrochemical platforms were washed with sterile water, and DPVs were recorded. The normalized signal obtained was interpolated in the calibration plot (Normalized intensity = 0.239 · log [S1 protein] + 0.0234; R² = 0.9971) and the recovery was calculated.

3. Results and discussion

The proposed aptasensor was developed following the procedure depicted in Scheme 1. The first step consists of the preparation of the nanostructured bioconjugate by combining FLB, synthesized tetrahedral DNA nanostructure containing the specific aptamer sequence of the SARS-CoV-2 S¹ protein (TDNapt) and Azure A (AA), that acts as an electrochemical indicator of the biorecognition reaction. The second stage is the aptasensor development by modifying CSPEs with the prepared nanostructured bioconjugate (FLB-TDNapt-AA). Then, the obtained sensing platform (CSPE/FLB-TDNapt-AA) is incubated with the SARS-CoV-2 S¹ protein (CSPE/FLB-TDNapt-AA/S1 protein) under the optimal conditions (37 °C, 1 h, using PBS 10.0 mM pH 7.0 as solvent). Finally, the biorecognition reaction is detected electrochemically by Differential Pulse Voltammetry using PB 0.1M pH 7.0 as electrolyte.

3.1. Nanostructured bioconjugate preparation and aptasensor development

The nanostructured bioconjugate was prepared following the steps of Scheme 1 and the procedure described in detail in the experimental section. Briefly, synthesized TDNapt and Azure A were incubated to favour the intercalative interaction of the AA with the TDNapt and form TDNapt-AA heterostructure. Then different steps of centrifugation were carried out to eliminate the AA molecules that did not interact with the



Scheme 1. Scheme followed for the nanostructured bioconjugate preparation (A) and aptasensor development (B).

DNA. The next step was the immobilization of the TDNapt-AA heterostructure on the FLB thanks to the Bi-S interaction between the bismuth of the bismuthene nanosheets and the sulphur atoms of the thiol group of the basal vertices of the TDNapt. All the steps of the nanobioconjugate preparation such as TDNapt concentration, volumes of FLB, TDNapt and AA were optimized, being optimal 1.00 μM of TDNapt and equal volume of FLB, TDNapt and AA (see Fig. S3). Once the nanostructured bioconjugate was prepared, an exhaustive characterization was carried out using different techniques such as spectrophotometry, fluorescence, and X-Ray photoelectron spectroscopy (XPS). Fig. 1 shows the UV-Visible (A) and fluorescence (B) spectra of the nanostructured bioconjugate (FLB-TDNapt-AA) as well as its precursors (FLB, AA and TDNapt). As can be observed in Fig. 1A, FLB does not show any absorption band (black line); however, in the case of SARS-CoV-2 aptamer-based tetrahedral DNA nanostructure (TDNapt, red line), a band at 258 nm, characteristic of the $\pi-\pi^*$ transition of the nitrogenous bases derived from the planar purine and pyrimidine (Rodger, 2013), are observed. The AA spectrum (blue line) shows the characteristic absorption bands of Azure A (AA); a

broad and intense band around 630 nm associated with the $n-\pi^*$ transitions of the C=N bond of the phenothiazine ring, and the narrower bands at 250 and 300 nm due to the $\pi-\pi^*$ transition of the phenothiazine ring (Martínez-Periñán et al., 2023). In the case of the TDNapt-AA and FLB-TDNapt-AA, green and purple lines, respectively, an absorbance spectrum quite similar to AA is observed, as the AA signals between 200 and 300 nm overlap with the TDNapt signals. The fluorescence spectra (Fig. 1B) show that for both, FLB and TDNapt, there is no fluorescence emission at all (black and red lines, respectively). In contrast, due to the fluorescent properties of the AA molecule, a broad band of emission (blue line) is observed around 650 nm when it is excited at 626 nm, characteristic of the phenothiazine ring of its structure. Again, the characteristic band of AA is observed in the case of TDNapt-AA (green line) and for the FLB-TDNapt-AA bioconjugate (purple line). In both cases, a displacement of the maximum emission at 665 nm and 670 nm (bathochromic effect) is registered due to the interaction between the AA and the DNA (Paul and Suresh Kumar, 2013). These results point to the formation of the nanostructured bioconjugate.

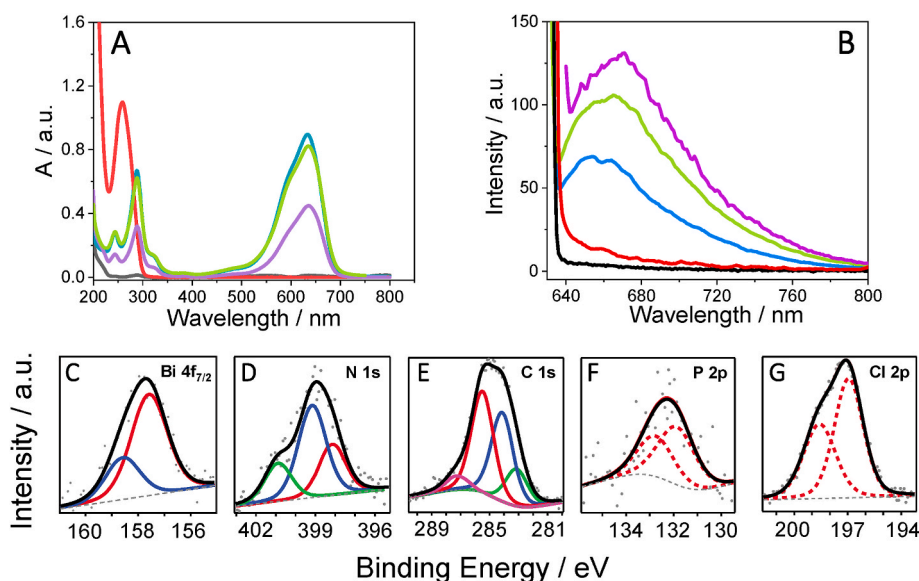


Fig. 1. UV-Visible spectra (A) and emission spectra (B) obtained at 626 nm excitation wavelength for: FLB (black line), TDNapt 500 nM in TM buffer solution (red line), Azure A 42.0 μM in water (blue line), TDNapt-AA 1:4 dilution in water (green line) and FLB-TDNapt-AA 1:4 dilution in water (purple line). XPS spectra for Bi 4f (C), Ni 1s (D), C 1s (E), P 2p (F) and Cl 2p (G). The incident photon energy was 1253.6 eV (Mg K α). XPS core levels are shown as dots, black lines correspond to the full fit, coloured lines indicate peak components and dashed lines indicate multiplets.

In order to confirm the results described above, the nanostructured bioconjugate was also characterized by XPS. FLB-TDNapt-AA bioconjugate was deposited on a gold substrate to ensure good electrical contact and binding energy calibration. Core level peaks of Bi, P, Cl, N, O and C were identified as contributions from the FLB, DNA and Azure A of the bioconjugate. No signs of unknown contamination were detected. In the case of Bi, the area corresponding to the Bi 4f_{7/2} core level was analyzed, where the deconvolution of the peak into two main components is observed, as shown in Fig. 1C. The first component (red line) at 158.6 eV corresponds to the reacted Bi that has lost some charge, it can be associated with a fraction of the Bi atoms interacting with the TDNapt, as the energy shift is smaller than the shift for Bi oxides or similar compounds (Torres et al., 2022). Then, a second slightly oxidized component (blue line) is found at 159.6 eV. For the N, the N 1s core level was qualitatively investigated due to the numerous N 1s contributions expected from TDNapt and Azure A (Fig. 1D). Deconvolution of the N 1s core level peak revealed three distinct components at 401.9 eV, 400.2

eV, and 399.2 eV. The last two low-energy components (red and blue lines) could be related to the TDNapt (Petrovykh et al., 2003; Ramstedt and Shchukarev, 2023). It is known that the Azure A molecule presents two N 1s components around 400 eV and 402 eV (Blacha-Grzechnik et al., 2015), so the components at 400.2 eV and 401.9 eV (blue and green lines, respectively) could be associated to the redox indicator. The shape on the line observed in Fig. 1D for the N 1s is then explained as a combination of both TDNapt and Azure A components. For the C, the C 1s core level was analyzed as shown in Fig. 1E, where four different components were found at 288.3 eV, 286.5 eV, 285.1 eV and 284.1 eV. The three higher binding energy components (purple, red, and blue lines respectively) correspond to the TDNapt and Azure A contributions (Blacha-Grzechnik et al., 2015, 2018; Ramstedt and Shchukarev, 2023). The small component at 284.1 eV (green line) is associated with adventitious carbon (Miller et al., 2002). The zone corresponding to the P 2p (see Fig. 1F) shows a unique component at 132.9 eV, characteristic of the P present in the TDNapt (Petrovykh et al., 2003; Ramstedt and

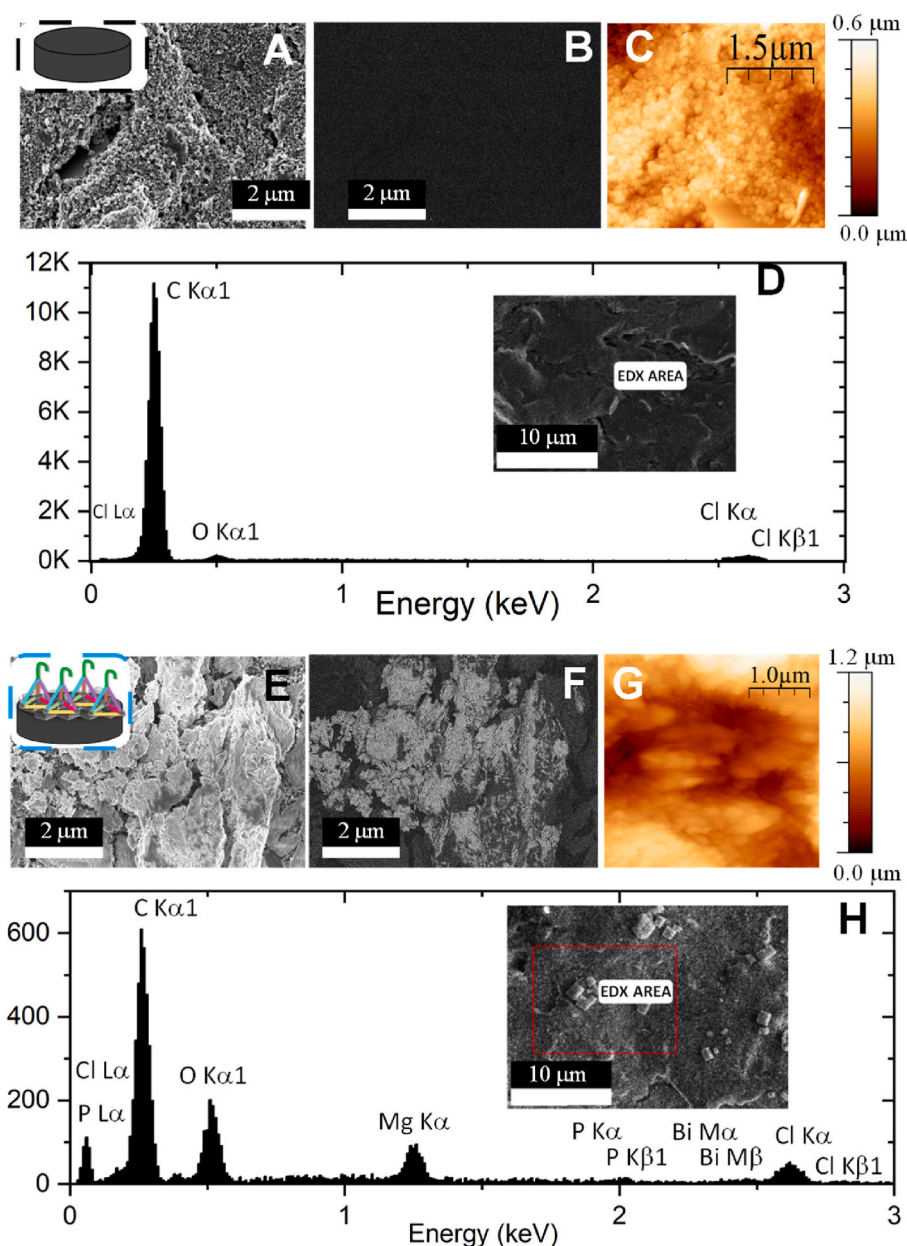


Fig. 2. Secondary electrons images (SEM) (A,E), Backscattered electrons images (BSE) (B,F), AFM (C,G) and EDX (D,H) of a CSPE electrode (A-D) and nanostructured bioconjugate immobilized on the CSPE electrode (E-H).

Shchukarev, 2023). Finally, the Cl 2p peak observed in Fig. 1G at 197.9 eV seems to confirm the presence of Azure A in the sample, but an important contribution from the TM buffer used in the synthesis of TDNapt can also be expected.

All these experiments confirm the presence of all the components (FLB, TDNapt and Azure A) on the nanostructured bioconjugate and prove the interactions between all of them, pointing out the correct preparation of the nanostructured bioconjugate.

As can be observed in Scheme 1, after nanostructured bioconjugate preparation, the next step in the aptasensor development is the immobilization of the nanostructured bioconjugate on the CSPE by drop casting. To confirm this modification different techniques such as scanning electron microscopy (SEM) with energy dispersive X-ray spectroscopy (EDX), atomic force microscopy (AFM), fluorescence microscopy and Raman spectroscopy were used. Fig. 2 shows the SEM (Fig. 2A, B, 2E and 2F) and AFM images (Fig. 2C and G) before (Fig. 2A–C) and after (Fig. 2E–G) bioconjugate immobilization on the CSPE. The AFM image of Fig. 2C depicts the characteristic CSPE surface, primarily composed of carbon grains ranging in size between 10 nm and 50 nm. Conversely, Fig. 2G illustrates the modified surface where the carbon grains are no longer distinguishable due to the deposition of larger agglomerates. Furthermore, the electrode surface is different when only FLB is immobilized on it (see Fig. S4 of SI). This can be due to the Bi–S interaction between the bismuth of the FLB and the sulphur of the thiol groups of the TDNapt (Alessio Verni et al., 2018; Romann et al., 2007; Yu et al., 2018).

In the backscattered electrons (BSE) images (Fig. 2B and F), different contrast areas corresponding to different materials are observed just on the nanostructured bioconjugate immobilized on the CSPE sample (see Fig. 2F). Areas of higher atomic number material show lighter color, which in this case corresponds to bismuthene, as confirmed by EDX (Fig. 2H and S4D). The BSE image of CSPE did not show any contrast (see Fig. 2B), implying the presence of just one type of material (carbon).

EDX was also used for the elemental characterization of the biosensing platform. Fig. 2D and H shows the results obtained. As can be observed, CSPE electrode shows the C characteristic peak of the carbon surface. After nanostructured bioconjugate immobilization (CSPE/FLB-TDNapt) new peaks associated with FLB and DNA phosphate backbone appear due to the nitrogenous bases of the TDNapt (see Fig. 2H), confirming nanostructured bioconjugate immobilization.

Fig. 3 shows the fluorescence microscopy images before and after nanostructured bioconjugate immobilization. As it can be observed after nanostructured bioconjugate immobilization, some fluorescent dots appear due to the Azure A molecules that are intercalated between the

nitrogenous bases of the TDNapt from the prepared FLB-TDNapt-AA bioconjugate. In order to confirm that this emission comes from the AA of the nanostructured bioconjugate, a fluorescence image of a CSPE after the modification with FLB was also taken. No emission was observed (Fig. S4F of SI). As controls, fluorescence images of CSPE/FLB-AA and CSPE/AA were also carried out. In both cases no emission fluorescence is observed probably due to the loss of AA in the washing steps, confirming the interaction of AA with DNA (TDNapt) and not with the electrode surface or FLB (Fig. S5 of SI).

Raman characterization of the CSPE before and after nanostructured bioconjugate immobilization is shown in Fig. S6 of SI. As it can be observed, CSPE (black line) shows the characteristic D and G bands of carbon at 1343 cm^{-1} and 1576 cm^{-1} (Pimenta et al., 2007). However, after its modification with the nanostructured bioconjugate (blue line), new bands appear at 100 cm^{-1} due to the two active Raman modes E_g and A_{1g} of FLB (see red line) and also bands at 392 cm^{-1} , 801 cm^{-1} and 1052 cm^{-1} that correspond to the vibrations of the DNA phosphate backbone. Moreover, bands at 516 cm^{-1} , 599 cm^{-1} , 761 cm^{-1} and 1151 cm^{-1} from the active Raman modes of adenine, guanine, cytosine, and thymine, respectively, are also observed (Prescott et al., 1984). These results confirm again nanostructured bioconjugate immobilization on the CSPE.

3.2. SARS-CoV-2 S¹ protein detection

After optimizing the preparation of the nanostructured bioconjugate and its immobilization on the biosensing platform, we evaluated the aptasensor ability to detect SARS-CoV-2 S¹ protein as a model of virus protein. Fig. 4B shows the Differential Pulse Voltammograms (DPVs) of the bare electrode (CSPE, black line) and the biosensing platform before (CSPE/FLB-TDNapt-AA, red line), and after the incubation with the analyte, the SARS-CoV-2 S¹ protein (CSPE/FLB-TDNapt-AA/S1 protein, blue line). As can be observed, there is no signal in the case of the bare electrode since there is no electroactive species on the electrode surface. On the other hand, both for the electrode before and after incubation with the S1 protein, the characteristic electrochemistry of Azure A can be followed with an oxidation peak at -0.5V . There is a clear difference in the current intensity before and after incubation, with a decrease in the anodic peak intensity in the presence of the protein that allows us to detect it. This decrease in the current intensity after the biorecognition reaction can be due to two factors. The first one corresponds to an increase in steric hindrance in the presence of the S1 protein, which hinders the electron transfer (Enebral-Romero et al., 2023; Erdem et al., 2022; Rahmati et al., 2021). On the other hand, it is well known that aptamers have a higher affinity, specificity, and selectivity to their target molecules than to complementary DNA sequences or other molecules, such as Azure A, that interact electrostatically and by intercalation with the nitrogenous bases of the aptamer DNA sequence. Therefore, when the biosensing platform is incubated with the SARS-CoV-2 S¹ protein, these intercalated Azure A molecules are displaced due to the specific biorecognition reaction between the aptamer and the protein (Abedi et al., 2023; Guo et al., 2015; Wang et al., 2023; Wu et al., 2019). This is evidenced by the intensity decrease recorded in the Differential Pulse Voltammogram (blue line, Fig. 4B) and the developed aptasensor's ability to detect the SARS-CoV-2 S¹ protein.

To confirm that the signal difference before and after incubation with the SARS-CoV-2 S¹ protein is due to a specific biorecognition reaction between the aptamer and the S1 protein, the biosensing platform was incubated with another non-specific protein (p53 protein) at the same concentration (200 fg mL^{-1}) (Scheme of Fig. 4A), and the signals obtained were compared, as shown in Fig. 4C. As can be observed in the presence of another non-specific protein, the response of the aptasensor developed did not change, which allows us to affirm that it is selective to the SARS-CoV-2 S¹ protein.

Once the preparation of the sensing platform was justified, the aptasensor response to different SARS-CoV-2 S¹ protein concentrations

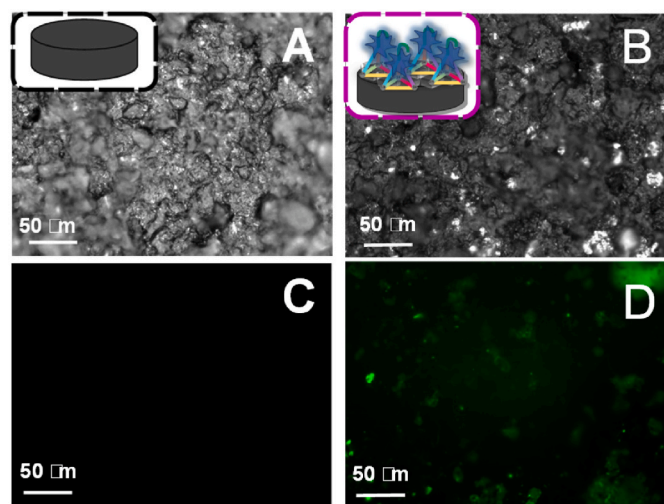


Fig. 3. Bright-field (A, B) and fluorescence (C, D) optical images of the carbon screen-printed electrode, CSPE (A, C) and CSPE/FLB-TDNapt-AA (B, D).

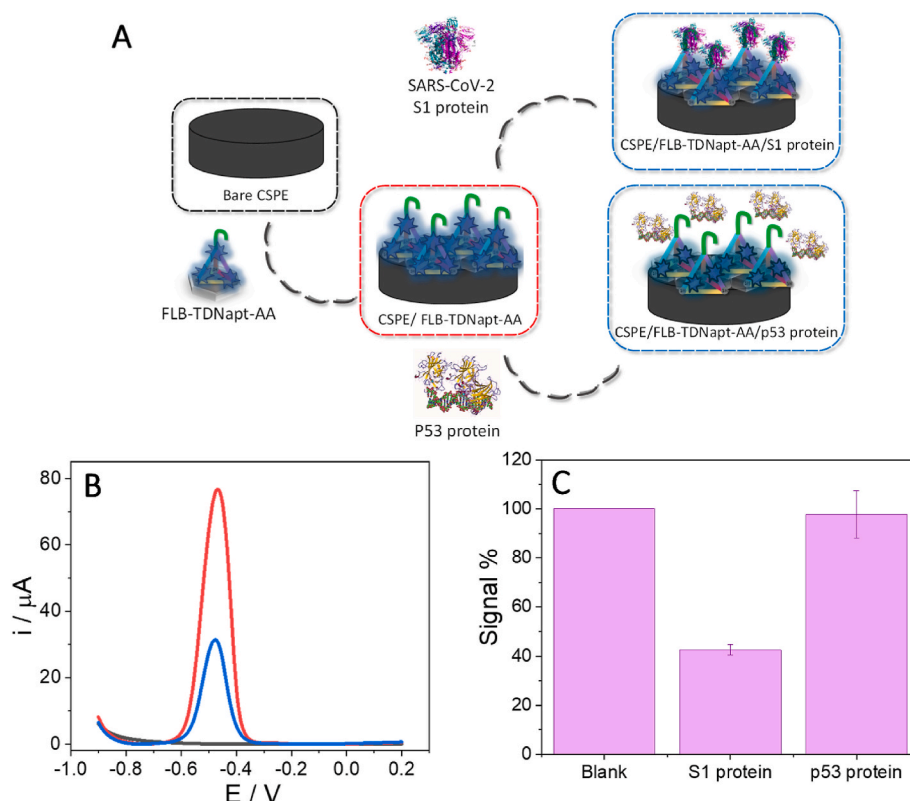


Fig. 4. Scheme of the process followed for the selectivity study (A). Differential Pulse Voltammogram (DPV) (B) obtained for: a bare CSPE (black line), CSPE/FLB-TDNapt-AA before (red line) and after the incubation with the SARS-CoV-2 S¹ protein (blue line) in PB 0.1M pH 7.0. Scan rate: 10 mV s⁻¹. Bar diagram of the % signal (C) obtained after incubating the CSPE/FLB-TDNapt-AA platform with the SARS-CoV-2 S¹ protein at 200 fg mL⁻¹ concentration and with the non-complementary p53 protein at the same concentration.

under the optimal experimental conditions described above was studied. For this purpose, the CSPE/FLB-TDNapt-AA platform was incubated with concentrations from 10.0 fg/mL to 1.00 pg/mL of S1 protein. Fig. 5A shows the calibration plot obtained representing the normalized electrochemical signal (with the blank, which is the signal before the incubation with the analyte) versus the logarithm of the S1 protein concentration. The normalized electrochemical signal is the absolute value of the difference in the signal after the incubation with S1 protein minus the blank, divided into the blank. An upward linear correlation between these two magnitudes fits the linear equation: Normalized intensity = $0.239 \cdot \log [S1 \text{ protein}] + 0.0234$ ($R^2 = 0.9971$). Values were obtained from the mean of three different concentration measurements, with a sensitivity of 0.239 a.u. log (fg⁻¹·mL) and a percentage coefficient of variation (CV) of 2.70%. The limits of detection (LOD) and

quantification (LOQ) were calculated from the formulas $y = X_B + 3 \cdot S_B$ and $y = X_B + 10 \cdot S_B$ (being X_B the mean of three times blank response and S_B the standard deviation), respectively, introducing the normalized intensity obtained in the calibration plot to estimate the S1 protein concentration. Statistical values of 1.74 fg mL⁻¹ and 10.7 fg mL⁻¹ were obtained for the LOD and LOQ, respectively, and experimentally assessed.

An interference study compared the aptasensor response to a 50.0 fg mL⁻¹ SARS-CoV-2 S¹ protein concentration in the presence of other interfering proteins at the same concentration (IgG, CEA, and p53). As shown in Fig. 5B, the response is not affected by the presence of other proteins, so the selectivity of the aptasensor for the SARS-CoV-2 S¹ protein is confirmed.

The stability of the aptasensor was also tested by measuring its

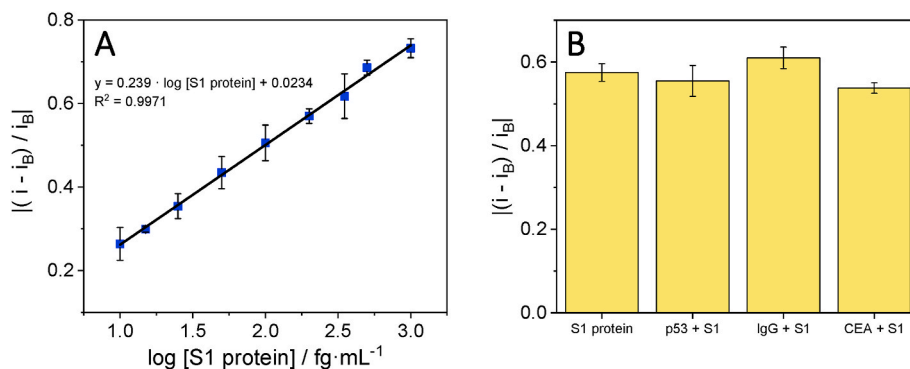


Fig. 5. Calibration curve (A) of the current intensity normalized signal obtained versus the logarithm of the SARS-CoV-2 S¹ protein concentration (from 10.0 fg mL⁻¹ to 1.00 pg mL⁻¹). Data are presented as mean \pm standard deviation ($n = 3$). Bar diagram (B) of the current intensity normalized signal obtained for 200 fg mL⁻¹ of SARS-CoV-2 S¹ protein in the presence of other interfering proteins, such as p53, IgG, and CEA, at the same concentration.

response to 50.0 fg mL^{-1} SARS-CoV-2 S¹ protein after 50 days stored at 4°C . The aptasensor response is constant and stable for 50 days, changing only 14% from the initial response (Fig. S7 in SI).

3.3. SARS-CoV-2 S¹ protein detection in nasopharyngeal swab samples

Given the interest in developing faster, simpler, and more sensitive detection techniques for the early detection of diseases caused by different pathogens and the good results obtained in the aptasensor developed for the detection of the SARS-CoV-2 virus in particular, we applied it to the detection of the SARS-CoV-2 S¹ protein in nasopharyngeal swab samples, with the aim of proposing an alternative methodology to the commercial antigen tests currently used. The process followed to prepare the sample is described in detail in the experimental section. The response to the non-spiked nasopharyngeal sample presents small differences ($\Delta i = 0.170 \mu\text{A}$) with the blank (CPSE/FLB-TDNapt-AA), due to the matrix effect of the sample. Recalculating for three different tests, the aptasensor response after the incubation with the nasopharyngeal sample spiked with S1 protein concentrations of 50.0 fg mL^{-1} and 100 fg mL^{-1} , recovery values of $(115 \pm 5) \%$ and $(122 \pm 10) \%$ were obtained, respectively. Based on these results, it is confirmed that the aptasensor developed can qualitatively and quantitatively detect the virus.

To demonstrate, among other advantages, the low limit of detection of our aptasensor, we compared the results obtained for the sample spiked with a S1 protein concentration of 50.0 fg mL^{-1} , with the result obtained for the same sample in a commercial antigen test, obtaining a negative response (see Fig. S8). These results demonstrate that the aptasensor is a potential alternative to the classical SARS-CoV-2 detection methods and as a new methodology for any pathogen detection.

Table S2 shows electrochemical aptasensors and biosensors described in the literature to detect SARS-CoV-2 virus. Analytical parameters of the aptasensor developed in this work compare well with those reported in the literature for similar platforms, showing better detection limit and proving that it can be an easy, simple and great practical alternative for SARS-CoV-2 virus detection (Amouzadeh Tabrizi and Acedo, 2022; Curti et al., 2022; Martínez-Periñán et al., 2021).

4. Conclusions

This work presents the development of a simple, fast, sensitive, and selective electrochemical aptasensor for virus detection. The aptasensor is based on a nanostructured bioconjugate preparation using few-layer bismuthene nanosheets, tetrahedral DNA nanostructures carrying the biorecognition element (specific aptamer of the S1 protein) and Azure A as redox indicator, and its immobilization on CSPE. As a proof of concept, SARS-CoV-2 S¹ RBD S1 protein was selected as analyte due to the great interest in developing new methodologies for its fast, simple, and efficient detection in order to avoid the spread of virus infections. The analytical properties of the aptasensor have been highly improved upon the TDNapt immobilization on the bismuthene hexagons via Bi-S interaction between the bismuth atoms and the thiol groups located in the tetrahedral basal vertices of the TDNapt. The aptasensor developed presents high selectivity, and stability, with a low limit of detection for SARS-CoV-2 S¹ protein of 1.74 fg mL^{-1} . The response is almost not affected by the presence of other potential interfering proteins and stable for 50 days. The real applicability of the aptasensor was proved by testing it to detect the S1 protein of the virus in nasopharyngeal swab samples spiked with different protein concentrations (50.0 and 100 fg mL^{-1}), obtaining recovery values of 115% and 122% , respectively. Hence, the aptasensor can be proposed as a potential alternative to the classical methodologies for pathogen detection.

CRedit authorship contribution statement

Estefanía Enebral-Romero: Writing – review & editing, Writing –

original draft, Methodology, Investigation, Formal analysis, Data curation. Daniel García-Fernández: Writing – review & editing, Writing – original draft, Investigation. Laura Gutiérrez-Gálvez: Writing – review & editing, Investigation. David López-Diego: Investigation. Mónica Luna: Writing – review & editing, Supervision, Resources, Project administration, Funding acquisition. Adrián García-Martín: Investigation. Elena Salagre: Investigation. Enrique G. Michel: Investigation. Íñigo Torres: Investigation. Félix Zamora: Writing – review & editing, Supervision, Resources, Project administration, Funding acquisition. Tania García-Mendiola: Writing – review & editing, Writing – original draft, Supervision, Resources, Project administration, Funding acquisition, Formal analysis, Data curation, Conceptualization. Encarnación Lorenzo: Writing – review & editing, Writing – original draft, Supervision, Resources, Project administration, Funding acquisition, Formal analysis, Data curation, Conceptualization.

Declaration of competing interest

The authors declare that they have no known competing financial interests or personal relationships that could have appeared to influence the work reported in this paper.

Data availability

Data will be made available on request.

Acknowledgements

This work has been financially supported by the Spanish Ministry of Economy and Competitiveness (PID2020-116728RB-I00, RED2022-134120-T), Spanish Ministry of Science, Innovation and Universities (TED2021-129738B-I00) and Community of Madrid (REACT-UE NANOCOV-CM, TRANSNANOAVANSENS, S2018/NMT-4349). Estefanía Enebral-Romero thanks the financial support of “Nanotecnología para detección del SARS-CoV-2 y sus variantes. NANOCOV” project and a contract as a predoctoral researcher funded by grant CEX2020-001039-S, supported by MCIN/AEI/10.13039/501100011033. Laura Gutiérrez-Gálvez was supported by a Formación del Profesorado Universitario (FPU) grant from the Spanish Ministry of Universities (FPU19/06309). Daniel García-Fernández and Adrián García-Martín were supported by a Programa Investigo grant from Autonomous Community of Madrid in the framework of the Plan de Recuperación, Transformación y Resiliencia financed by the European Union – NextGenerationEU (09-PIN1-00013.4/2022- 83rd and 66rd place, respectively). The authors acknowledge the support of the European Union (EU) and Horizon 2020 through Instruct Proposal PID: 21859, and the CRIOMECORR project (ESFRI-2019-01-CSIC-16) to the cryoEM CNB-CSIC facility.

F. Z. acknowledges financial support from the Spanish Ministry of Science and Innovation, through the “María de Maeztu” Programme for Units of Excellence in R&D (CEX2023-001316-M, PDC2021-120782-C21, and PID2022-138908NB-C31), the “(MAD2D-CM)-UAM” project funded by Comunidad de Madrid, by the Recovery, Transformation and Resilience Plan, and by NextGenerationEU from the European Union. F. Z. also acknowledges support from the European Innovation Council under grant Agreement 101047081 (EVA).

EGM acknowledges financial support from the Spanish Ministry of Science and Innovation, through the “María de Maeztu” Programme for Units of Excellence in R&D (CEX2018-000805-M) and through grant PID2021-123295NB-I00.

We also acknowledge María U. González help with Fluorescence Microscopy and the service from the MiNa Laboratory at IMN, and funding from CM (project S2018/NMT-4291 TEC2SPACE), MINECO (project CSIC13-4E-1794) and EU (FEDER, FSE).

Appendix A. Supplementary data

Supplementary data to this article can be found online at <https://doi.org/10.1016/j.bios.2024.116500>.

References

- Abedi, R., Raouf, J.B., Mohseni, M., Bagheri Hashkavayi, A., 2023. *Microchim. Acta* 190, 308.
- Ahmadivand, A., Gerislioglu, B., 2022. *Laser Photon. Rev.* 16, 2100328.
- Alessio Verni, G., Long, B., Gity, F., Lanius, M., Schüffegen, P., Mussler, G., Grützmacher, D., Greer, J., Holmes, J.D., 2018. *RSC Adv.* 8, 33368–33373.
- Amouzadeh Tabrizi, M., Acedo, P., 2022. *Biosens. Bioelectron.* 215, 114556.
- Bai, L., Yuan, R., Chai, Y., Yuan, Y., Wang, Y., Xie, S., 2012. *Chem. Commun.* 48, 10972.
- Blacha-Grzechnik, A., Piwowar, K., Koscielniak, P., Kwoka, M., Szuber, J., Zak, J., 2015. *Electrochim. Acta* 182, 1085–1092.
- Blacha-Grzechnik, A., Piwowar, K., Zdyb, T., Krzywiecki, M., 2018. *Appl. Surf. Sci.* 457, 221–228.
- Bujold, K.E., Lacroix, A., Sleiman, H.F., 2018. *Chem* 4, 495–521.
- Curti, F., Fortunati, S., Knoll, W., Giannetto, M., Corradini, R., Bertucci, A., Careri, M., 2022. *ACS Appl. Mater. Interfaces* 14, 19204–19211.
- Enebral-Romero, E., Gutiérrez-Gálvez, L., Del Caño, R., Sulleiro, M.V., Naranjo, A., Gómez, I.J., Pariente, F., Pérez, E.M., García-Mendiola, T., Lorenzo, E., 2023. *Sensor. Actuator. B Chem.* 392, 134105.
- Erdem, A., Senturk, H., Yildiz, E., Maral, M., 2022. *Diagnostics* 12, 1992.
- García Fernández, D., Gutiérrez Gálvez, L., Vázquez Sulleiro, M., Garrido, M., López-Diego, D., Luna, M., Pérez, E.M., García-Mendiola, T., Lorenzo, E., 2023. *Talanta*, 125497.
- Gimeno, A., Ares, P., Horcas, I., Gil, A., Gómez-Rodríguez, J.M., Colchero, J., Gómez-Herrero, J., 2015. *Bioinformatics* 31, 2918–2920.
- Guo, Y., Wang, X., Sun, X., 2015. *Int. J. Electrochem. Sci.* 10, 3668–3679.
- Gutiérrez-Gálvez, L., García-Fernández, D., Barrio, M.D., Luna, M., Torres, I., Zamora, F., Navío, C., Milán-Rois, P., Castellanos, M., Abreu, M., Cantón, R., Galán, J.C., Somoza, Á., Miranda, R., García-Mendiola, T., Lorenzo, E., 2024. *Talanta* 269, 125405.
- Hameed, S., Xie, L., Ying, Y., 2018. *Trends Food Sci. Technol.* 81, 61–73.
- Hartati, Y.W., Syahrani, S., Gaffar, S., Wyantuti, S., Yusuf, M., Subroto, T., 2021. *Indones. J. Chem.* 21, 1526.
- Horcas, I., Fernández, R., Gómez-Rodríguez, J.M., Colchero, J., Gómez-Herrero, J., Baro, A.M., 2007. *Rev. Sci. Instrum.* 78, 013705.
- Li, Y.-L., Xie, F.-T., Yao, C., Zhang, G.-Q., Guan, Y., Yang, Y.-H., Yang, J.-M., Hu, R., 2022. *Analyst* 147, 4578–4586.
- Lo, P.K., Karam, P., Aldaye, F.A., McLaughlin, C.K., Hamblin, G.D., Cosa, G., Sleiman, H. F., 2010. *Nat. Chem.* 2, 319–328.
- Martínez-Periñán, E., Domínguez-Saldaña, A., Villa-Manso, A.M., Gutiérrez-Sánchez, C., Revenga-Parra, M., Mateo-Martí, E., Pariente, F., Lorenzo, E., 2023. *Sensor. Actuator. B Chem.* 374, 132761.
- Martínez-Periñán, E., García-Mendiola, T., Enebral-Romero, E., del Caño, R., Vera-Hidalgo, M., Vázquez Sulleiro, M., Navío, C., Pariente, F., Pérez, E.M., Lorenzo, E., 2021. *Biosens. Bioelectron.* 189, 113375.
- Miller, D.J., Biesinger, M.C., McIntyre, N.S., 2002. *Surface & Interface Analysis*, 33, pp. 299–305.
- Mishra, A., Pilloton, R., Jain, S., Roy, S., Khanuja, M., Mathur, A., Narang, J., 2022. *Biosensors* 12, 88.
- Mugo, S.M., Alberkant, J., Bernstein, N., Zenkina, O.V., 2021. *Anal. Methods* 13, 4169–4173.
- Nehra, M., Kumar, V., Kumar, R., Dilbaghi, N., Kumar, S., 2022. *Biosensors* 12, 489.
- Nemes-Incze, P., Osváth, Z., Kamarás, K., Biró, L.P., 2008. *Carbon* 46, 1435–1442.
- Paul, P., Suresh Kumar, G., 2013. *Spectrochim. Acta Mol. Biomol. Spectrosc.* 107, 303–310.
- Petrovykh, D.Y., Kimura-Suda, H., Whitman, L.J., Tarlov, M.J., 2003. *J. Am. Chem. Soc.* 125, 5219–5226.
- Pimenta, M.A., Dresselhaus, G., Dresselhaus, M.S., Cançado, L.G., Jorio, A., Saito, R., 2007. *Phys. Chem. Chem. Phys.* 9, 1276–1290.
- Pina-Coronado, C., Martínez-Sobrinho, Á., Gutiérrez-Gálvez, L., Del Caño, R., Martínez-Periñán, E., García-Nieto, D., Rodríguez-Peña, M., Luna, M., Milán-Rois, P., Castellanos, M., Abreu, M., Cantón, R., Galán, J.C., Pineda, T., Pariente, F., Somoza, Á., García-Mendiola, T., Miranda, R., Lorenzo, E., 2022. *Sensor. Actuator. B Chem.* 369, 132217.
- Prescott, B., Steinmetz, W., Thomas, G.J., 1984. *Biopolymers* 23, 235–256.
- Rahmati, Z., Roushani, M., Hosseini, H., Choobin, H., 2021. *Microchim. Acta* 188, 105.
- Ramstedt, M., Shchukarev, A., 2023. *Surf. Sci. Spectra* 30, 014011.
- Rodger, A., 2013. *Encyclopedia of Biophysics*. Springer, Berlin Heidelberg, Berlin, Heidelberg, pp. 2714–2718.
- Romann, T., Grozovski, V., Lust, E., 2007. *Electrochem. Commun.* 9, 2507–2513.
- Rothmund, P.W.K., 2006. *Nature* 440, 297–302.
- Roushani, M., Shahdost-fard, F., 2017. *Mater. Sci. Eng. C* 75, 1091–1096.
- Schmid, M., Steinrück, H., Gottfried, J.M., 2014. *Surface & Interface Analysis*, 46, pp. 505–511.
- Su, S., Sun, Q., Gu, X., Xu, Y., Shen, J., Zhu, D., Chao, J., Fan, C., Wang, L., 2019. *TrAC, Trends Anal. Chem.* 119, 115610.
- Torres, I., Villa-Manso, A.M., Revenga-Parra, M., Gutiérrez-Sánchez, C., Aldave, D.A., Salagre, E., Michel, E.G., Varela, M., Gómez-Herrero, J., Lorenzo, E., Pariente, F., Zamora, F., 2022. *Appl. Mater. Today* 26, 101360.
- Wang, L.-Y., Chen, J.-S., Liu, X.-P., Mao, C.-J., Jin, B.-K., 2023. *Talanta* 253, 123988.
- Wang, Y., Wang, F., Han, Z., Huang, K., Wang, X., Liu, Z., Wang, S., Lu, Y., 2020. *Sensor. Actuator. B Chem.* 304, 127418.
- Wu, H., Li, M., Wang, Z., Yu, H., Han, J., Xie, G., Chen, S., 2019. *Anal. Chim. Acta* 1049, 74–81.
- Yu, N., Wang, Z., Zhang, J., Liu, Z., Zhu, B., Yu, J., Zhu, M., Peng, C., Chen, Z., 2018. *Biomaterials* 161, 279–291.
- Zambry, N., Ahmad Najib, M., Awang, M., Selvam, K., Khalid, M., Bustami, Y., Hamzah, H., Ozsoz, M., Abd Manaf, A., Aziah, I., 2022. *Diagnostics* 12, 3186.